our previous study [18]. In the present study, R and H were considered to be the same as those of the previous study, i.e., 16 and 5 nm, respectively. When the observed structure was ring-like, the distance between two peak heights based on the cross sections was measured and was regarded as being its diameter.

Image analysis was performed with NanoScope v7.00 (Veeco, Santa Barbara, CA, USA) and data analyses, i.e., statistical analysis and Gaussian fit, were performed with IGOR Pro v6.0.3 (WaveMetrics, Lake Oswego, OR, USA). The Gaussian fit is given by:

$$f(x) = y_0 + A\exp\left\{(x - x_0)^2/(x_{width})^2\right\} \quad (2)$$

where y_0 is the base line, A is the amplitude, x_0 is the estimated peak position, and x_{width} is the full width at half maximum of the fitting curve.

Observation by AFM of Qdots on mica

Freshly cleaved mica was incubated with 50 μl of 0.5% (*w/v*) poly-L-lysine (MW=1,000–4,000; Sigma-Aldrich, St. Louis, MO, USA) in PBS. After 1 min adsorption, the mica was washed with Mill-Q water three times and dried at room temperature. Then, Qdots were prepared in PBS at a dilution of 1:1,000. A 100-μl solution of Qdots was deposited on the poly-L-lysine-coated mica and allowed to adsorb for 20 min. The supernatant was then removed and the mica was rinsed gently with 200 μl of Milli-Q water three times. After the sample was air-dried at room temperature, it was immediately imaged by AFM. To analyze the size and number of Qdots, first, the obtained image was converted into grayscale AFM images, the intensity value of which ranged from 0 (black) to 255 (white), by using Adobe Photoshop 6.0 (Adobe Systems, San Jose, CA, USA). The number of Qdots was counted by the command "Analyze particles" of ImageJ v1.32j (NIH, Bethesda, MD, USA) and their heights were then analyzed by the use of a command "section" of NanoScope v4.23. Every extracted structure was subjected to height analysis to prevent experimenter bias.

Results

Prestin labeling with Qdots and low-magnification AFM images

Evaluating the expression of prestin in the transfected CHO cells, the fluorescence of GFP, coexpressed with prestin in such cells, was observed since the GFP fluorescence is positively correlated with the expression of prestin in the prestin-transfected CHO cells [26]. Figure 1 shows the GFP fluorescence of the prestin-transfected and untransfected CHO cells. GFP fluorescence was detected in the prestin-transfected cells (top middle panel), indicating the expres-

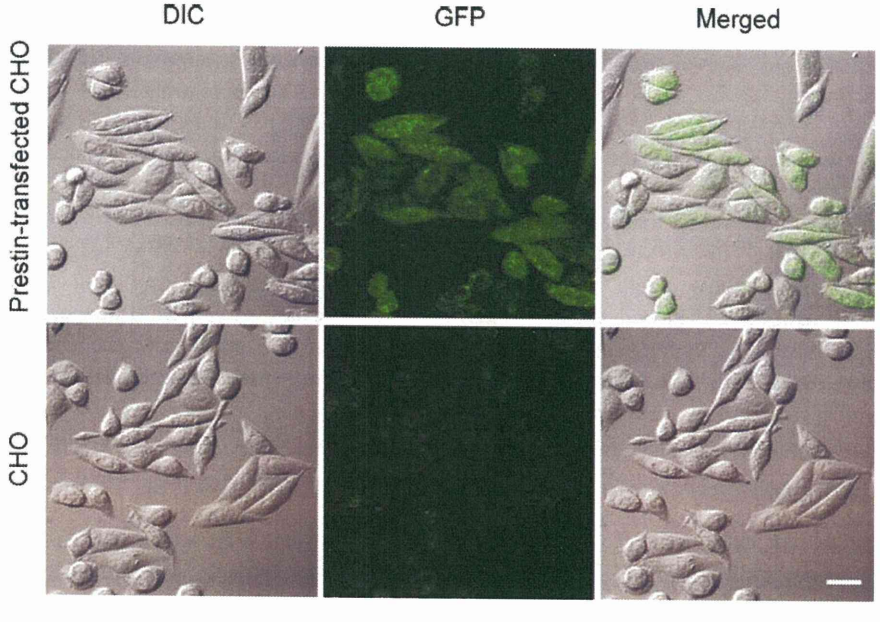

Fig. 1 GFP fluorescence of the prestin-transfected and untransfected CHO cells. *Left panels* differential interference contrast (*DIC*) images, *middle panels* GFP fluorescence images, *right panels* merged images. GFP fluorescence was detected in the prestin-transfected cells (*top middle panel*), indicating the expression of prestin in the cells. By contrast, GFP fluorescence was not observed in the untransfected CHO cells (*bottom middle panel*). Scale bar is 20 μm

sion of prestin in the cells. By contrast, GFP fluorescence was not observed in the untransfected CHO cells (bottom middle panel).

Figure 2a shows the prestin labeling with Qdots and the corresponding low-magnification AFM images of the isolated plasma membranes of a prestin-transfected CHO cell and those of an untransfected CHO cell. Prestin labeling (red), which labels the N terminus of prestin, was observed in the isolated plasma membrane of the prestin-transfected CHO cell (top left panel); by contrast, it was not observed in the isolated plasma membrane of the untransfected CHO cell (top right panel). These results indicate the presence of prestin in the isolated plasma membranes of the prestin-transfected CHO cell even after the plasma membranes were isolated by gentle exposure to the hypotonic buffer and incubated with the high-salt buffer and trypsin. Low-magnification AFM images are shown in the bottom panels in Fig. 2a. The surface topologies of

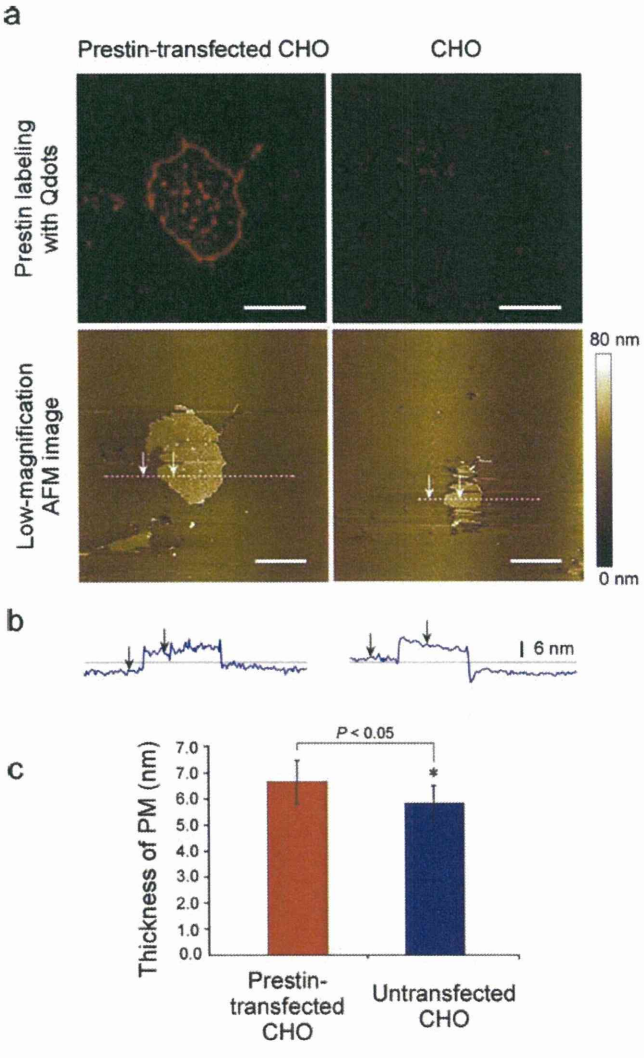

Fig. 2 Isolated plasma membranes of the prestin-transfected and untransfected CHO cells. **a** Fluorescence images of prestin labeled with Qdots and the corresponding low-magnification AFM images. Prestin labeling (*red*), which labels the N terminus of prestin, was observed in the isolated plasma membrane of the prestin-transfected CHO cell, but not observed in the isolated plasma membrane of the untransfected CHO cell. Low-magnification AFM images indicated that the surface topologies of the cytoplasmic faces of the prestin-transfected and untransfected CHO cells were flat at this magnification. Scale bars are 10 μm. **b** The cross sections of the isolated plasma membranes along the *dotted line* shown in the *bottom panels* of **a**. Height difference between the *arrows*, each horizontal distance of which was 6 μm, was measured as the thickness of the isolated plasma membrane. **c** Mean and standard deviation of the thickness of the isolated plasma membranes. The average thickness of the isolated plasma membranes of the prestin-transfected CHO cells was 6.65± 0.83 nm (n=16) and that of the untransfected CHO cells was 5.83± 0.67 nm (n=9). The thickness of the isolated plasma membranes showed statistically significant difference between the prestin-transfected and untransfected CHO cells, as indicated by the *asterisk* (P< 0.05, Student's t test)

the cytoplasmic faces of both prestin-transfected and untransfected CHO cells seem to be flat at this magnification. Figure 2b shows the cross sections of the isolated plasma membranes along the dotted line shown in the bottom panels of Fig. 2a. Height difference between the arrows shown in the figures, each horizontal distance of which was 6 μm, was measured as the thickness of the isolated plasma membrane. The mean and standard deviation of the thickness of the different isolated plasma membranes of the prestin-transfected and untransfected CHO cells are shown in Fig. 2c. The average thickness of the isolated plasma membranes of the prestin-transfected CHO cells was 6.65±0.83 nm (n=16) and that of the untransfected CHO cells was 5.83±0.67 nm (n=9). The thickness of the isolated plasma membrane showed statistically significant difference between the prestin-transfected and untransfected CHO cells, as indicated by the asterisk (P<0.05, Student's t test).

Low-, middle-, and high-magnification AFM images

The cytoplasmic surfaces of the isolated plasma membranes of the prestin-transfected CHO cells and those of the untransfected CHO cells were observed by the tapping mode of AFM.

Figure 3 is a fluorescence image of prestin labeled with Qdots in the prestin-transfected CHO cell (Fig. 3a) and the corresponding AFM images at low- (Fig. 3b) and middle-magnifications (Fig. 3c). The inset in each image is the digital zoom of the boxed area in each image. The middle-magnification image (Fig. 3c) was obtained from the boxed area in Fig. 3b. As shown in Fig. 3a, the distribution of prestin labeling with Qdots in the plasma membrane of the prestin-transfected CHO cell was seen as a pattern of bright patches, as indicated by the arrowheads in its inset. The fluorescence of Qdots in the area surrounding the patches but not in the substrate area (asterisk, Fig. 3a) was also observed although its intensity was weak, indicating that prestin is nonuniformly distributed all over the plasma membrane of CHO cells. In the low-magnification AFM image (Fig. 3b), the smooth surface of the cytoplasmic face of prestin-transfected CHO cells was confirmed. However, as shown in its digital-zoomed image (inset, Fig. 3b), bulges about 7 nm in height were observed, as shown by the arrowheads. Comparison between the digital-zoomed images of Fig. 3a and b reveals that the location of the bright patches of Qdot labeling and the bulges are colocalized. Furthermore, by comparing the digital-zoomed image of Fig. 3b with c, the bulges seen in Fig. 3b (dotted circles) corresponded to the small bumps seen in Fig. 3c (dotted circles).

Figure 4 shows the high-magnification AFM images of the boxed area of Fig. 3c. In these images, particles about 8 nm in height were observed as shown by the arrows. No changes in the location of these particles were observed between the scanning from the top to the bottom (Fig. 4a) and the subsequent scanning from the bottom to the top (Fig. 4b).

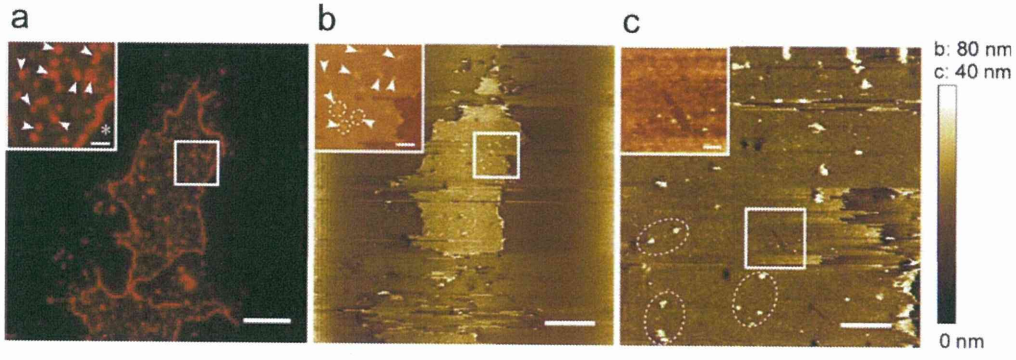

Fig. 3 Fluorescence image of prestin labeled with Qdots and the corresponding AFM images of the prestin-transfected CHO cell. **a** Fluorescence image of prestin labeled with Qdots. The *inset* shows a digital-zoomed image of the *boxed area*. **b** AFM image at low magnification. The *inset* is the digital zoom of the *boxed area*. **c** Middle-magnification AFM image obtained from the *boxed area* shown in **b**. The *inset* shows the digital zoom of the *boxed area*. As shown in **a**, the distribution of prestin labeling with Qdots in the plasma membrane of the prestin-transfected CHO cell was seen as a pattern of bright patches, as indicated by the *arrowheads* in its *inset*. As well as from such bright patches, fluorescence of Qdots was also detected from all over the plasma membrane while it was not observed in the substrate area (*asterisk*), indicating that prestin was nonuniformly distributed all over the plasma membrane of CHO cells. In the low-magnification AFM image (**b**), the smooth surface of the cytoplasmic face of prestin-transfected CHO cells was confirmed. However, as shown in its digital-zoomed image, the bulges about 7 nm in height were observed, as shown by the *arrowheads* in its *inset*. Comparison between the digital-zoomed images of **a** and **b** revealed that the location of the bright patches of Qdot labeling and the bulges were colocalized. Furthermore, by comparing the digital-zoomed image of **b** with **c**, the bulges indicated by *dotted circles* in **b** were found to correspond to the small bumps indicated by *dotted circles* in **c**. Scale bars of **a**, **b**, and **c** are 10, 10, and 2 μm, respectively. Scale bars of the insets of **a**, **b**, and **c** are 2 μm, 2 μm, and 500 nm, respectively

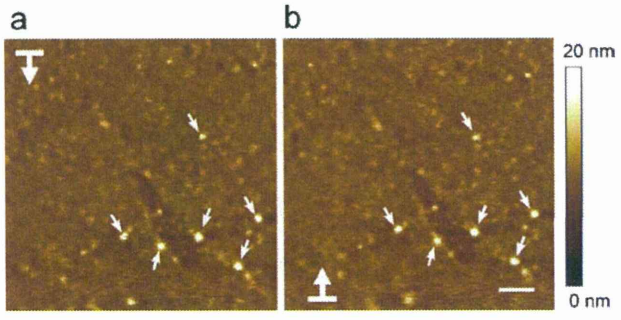

Fig. 4 High-magnification AFM images of the *boxed area* of Fig. 3c. **a** Image obtained by scanning from the top to the bottom of the sample. **b** Image obtained by scanning from the bottom to the top of the sample. In these images, particles about 8 nm in height were observed, as indicated by the *arrows*. No changes in the location of these particles were observed between **a** and **b**. Scale bar is 300 nm

Figure 5 indicates the AFM images of the isolated plasma membranes of the untransfected CHO cell at different magnifications. Low-, middle-, and high-magnification AFM images are shown by Fig. 5a,b, and c, respectively. The middle-magnification image (Fig. 5b) was obtained from the boxed area in Fig. 5a. The high-magnification image (Fig. 5c) was obtained from the boxed area in Fig. 5b. In the high-magnification image, although there are a few accumulations more than 15 nm in height, no other obvious structures are seen.

Observation by AFM of Qdots on mica and the plasma membrane

In this study, Qdots were used as topographic surface markers. To confirm the shape of Qdots, they were adsorbed on freshly cleaved mica coated with poly-L-lysine and immediately scanned by AFM. Figure 6a shows the Qdots adsorbed on mica. Uniform particles about 8 nm in height were observed. The frequency distribution of the Qdots on mica (red, n=45) is shown in Fig. 6b, along with such distribution of the Qdots observed on the plasma membranes of the prestin-transfected CHO cells (blue, n=78), which label prestin molecules due to an antigen–antibody reaction. This histogram exhibited Gaussian distributions for both data sets (red, y_0=0.6±2.2, A=9.6±2.3, x_{width}=0.7±0.2; blue, y_0=−2.1±7.5, A=8.2±7.1, x_{width}=2.9±2.2). The peaks of the Qdots observed on mica and on the isolated plasma membranes were 8.2±0.1 nm and 7.9±0.3 nm, respectively. The mean and standard deviations of the heights of Qdots observed on mica and the isolated plasma membranes are shown in Fig. 6c. The average height of the Qdots on mica was 8.2±0.5 nm and that observed on the plasma membranes of the prestin-transfected CHO cells was 7.9±1.3 nm. These two sizes of Qdots were statistically identical (P>0.05, Student's t test).

Figure 7a shows a high-magnification AFM height image of the isolated plasma membrane of the prestin-transfected CHO cell, the prestin molecules of which were labeled with Qdots. Different sizes of particles are observed in the height image. Figure 7b shows the phase image of a. Figure 7c indicates the cross sections of the phase images of particles A and B obtained between α and α′, and β and β′ (arrowheads), respectively. As shown in these figures, a bright phase contrast (positive phase shift) was observed at the center of particle B while a dark phase contrast (negative phase shift) was observed at its periphery. By contrast, such phase shifts were not observed for particle A.

Prestin topology in the isolated plasma membranes of CHO cells

Figure 8 shows high-magnification 3-D AFM images of a prestin-transfected CHO cell. Qdots 8 nm in height were clearly observed on the cytoplasmic face of the isolated plasma membrane of the prestin-transfected CHO cell, as indicated by black arrowheads. As shown in the magnification in the right of Fig. 8a, a ring-like structure with four

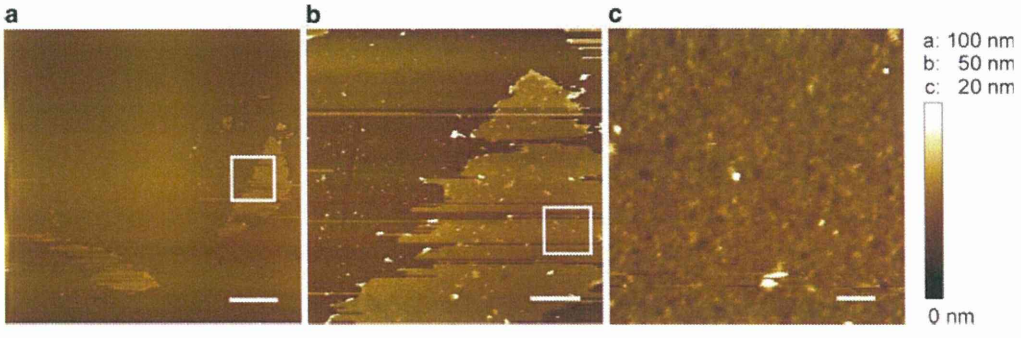

Fig. 5 AFM images of isolated plasma membranes of an untransfected CHO cell at different magnifications. **a** Low-magnification image. **b** Middle-magnification image obtained from the *boxed area* shown in **a**. **c** High-magnification image obtained from the *boxed area* shown in **b**. In the high-magnification image, although there are a few accumulations more than 15 nm in height, no other obvious structures are seen. Scale bars of **a**, **b**, and **c** are 10 μm, 2 μm, and 300 nm, respectively

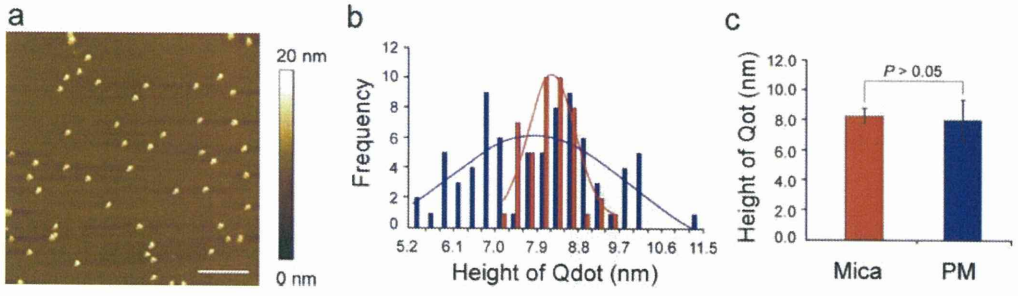

Fig. 6 The Qdots adsorbed on the freshly cleaved mica coated with poly-L-lysine. **a** AFM image. Uniform particles about 8 nm in height were observed. Scale bar is 200 nm. **b** Frequency distribution of the Qdots on mica and on the isolated plasma membranes of prestin-transfected CHO cells. *Red bars* show the frequency distribution of the Qdots on mica (n=45) and *blue bars* show such distribution of the Qdots on the plasma membranes of the prestin-transfected CHO cells, which label prestin molecules due to the antigen–antibody reaction (n=78). These histograms exhibited Gaussian distributions for both data sets, as shown by *red* and *blue lines* (red, y_0=0.6±2.2, A=9.6±2.3, x_{width}=0.7±0.2; blue, y_0=−2.1±7.5, A=8.2±7.1, x_{width}=2.9±2.2). The peaks of the former and the latter were 8.2±0.1 and 7.9±0.3 nm, respectively. **c** Mean and standard deviations of the heights of Qdots observed on mica and the isolated plasma membranes. The average height of the Qdots on mica was 8.2±0.5 nm and that observed on the plasma membranes of the prestin-transfected CHO cells was 7.9±1.3 nm. These two sizes of Qdots were statistically identical (P>0.05, Student's t test)

peaks and one valley at its center, possibly corresponding to a prestin molecule, was observed in the vicinity of the Qdot (A, arrow). In the vicinity of the other Qdots, similar structures were observed at the locations indicated by arrows (A–D), the magnifications of which are shown in the bottom panels.

Figure 8b shows examples of 3-D images of the structures observed in the vicinity of the Qdots. These images were obtained from the different cells shown in Fig. 8a. Most of the observed structures are ring-like structures with a depression surrounded by four peaks (E–K). In some cases, such structures are adjacent to the others, forming a unit with two molecules (L). Besides those ring-like structures, a square-shaped structure with a protrusion at its center, four corners of which are indicated by arrowheads, was also observed (M). The side length of the square, i.e., the length between the adjacent corners indicated by arrowheads, was 7.7 nm and the diameter of the protrusion was 6.2 nm, derived from Eq. 1.

Figure 8c indicates the frequency distribution of the diameter of the ring-like structures (n=120). In the present study, we observed the cytoplasmic faces of the plasma

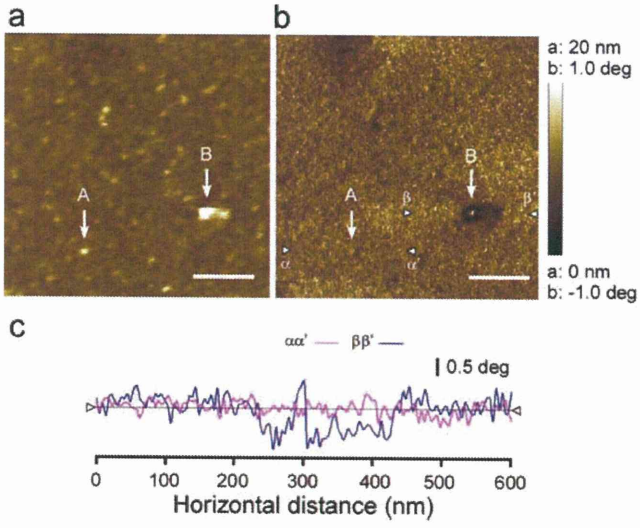

Fig. 7 Height and phase AFM images of the isolated plasma membrane of the prestin-transfected CHO cell incubated with antiprestin antibody and Qdot-conjugated secondary antibody. **a** High-magnification height image. Different sizes of particles are observed (*A* and *B*, *arrows*). **b** Phase image of **a**. **c** Cross sections of phase images of the particles *A* and *B* (between α and α' and β and β', *arrowheads*). Regarding particle *B*, a bright phase contrast (positive phase shift) was observed at the center of the particle while a dark phase contrast (negative phase shift) was observed at its periphery. By contrast, such phase shifts were not observed for particle *A*. Scale bars are 300 nm

membranes isolated from 23 prestin-transfected CHO cells and found 109 Qdots on such membranes. Since, in some cases, a few ring-like structures were found around one Qdot, 120 such structures were found in total. This histogram exhibited two main Gaussian distributions shown by red and blue lines (red, y_0=0.9±1.0, A=6.2±2.1, x_{width}=0.5±0.2; blue, y_0=1.6±0.7, A=4.6±1.2, x_{width}=1.4±0.5). The peaks of those distributions were 9.6±0.1 nm (red) and 13.0±0.2 nm (blue), respectively.

Discussion

Sample preparation

In our previous study, the cytoplasmic surfaces of the isolated plasma membranes of CHO cells were found to be covered with protruding globular structures approximately 100 nm in diameter [18]. These protruding globular structures were colocalized with the immunofluorescence of prestin, indicating that prestin was not uniformly distributed in the plasma membrane of the prestin-transfected CHO cells. As these large structures hinder efforts to obtain AFM images at high-magnification, the images were obtained in the membrane areas without such structures in that study. In the present study, to observe the membrane topology of prestin at the nanoscale level, a flatter surface of the isolated plasma membrane was required. To obtain such flat plasma membrane sheets, therefore, the sample preparation method was modified. That is, the CHO cells were cultured in the culture medium overnight, rather than 5 min incubation in the external solution just before sonication as in the previous method. Due to this, the cell shape became flatter and more spindly, as shown in Fig. 1, compared with the cells grown by the previous method. As shown in the bottom panels of Fig. 2a, this procedure significantly reduced the number of the protruding globular structures 100 nm in diameter on the cytoplasmic faces of the isolated plasma membranes of the CHO cell.

The existence of prestin in the plasma membrane isolated from such spindle-shaped CHO cells after incubation with high-salt buffer and trypsin was confirmed by immunostaining (top panels, Fig. 2). Fluorescence labeling of the prestin-transfected CHO cells but not of the untransfected CHO cells was confirmed, suggesting that prestin existed in the isolated plasma membranes of the spindle-shaped CHO cells even after treatment with high-salt buffer and trypsin, and thus these isolated plasma membranes were applicable as samples for AFM observation.

As shown in Fig. 2c, the average thickness of the isolated plasma membranes of the prestin-transfected CHO cells was larger than that of the untransfected CHO cells by 0.82 nm with statistical significance, as shown by the asterisk (P<0.05, Student's t test). Mitra et al. [27] demonstrated that the thickness of the biological membranes was reduced up to 5 Å by depletion of the membrane proteins. Based on this report, it is likely that the increase in the thickness of the isolated plasma membrane of the prestin-transfected CHO cells in the present study was possibly due to the expression of prestin molecules.

As shown in the inset of Fig. 3a, the distribution of prestin in the plasma membrane of the CHO cells was not uniform; rather, a large amount of prestin was distributed in many spots and residual prestin was distributed in the area surrounding those spots. This distribution pattern of prestin is consistent with that observed in our previous study [18]. In that study, a considerable amount of prestin was formed to be aggregated in protruding globular structures 100 nm in diameter, which were rich in phospholipids, indicating the possible occurrence of assembly and/or disassembly of the vesicle. However, as mentioned above, in the present study, there were no such 100 nm protruding globular structures. Instead, as shown in the digital-zoomed image in Fig. 3b, the bulges about 7 nm in height were observed. By comparing the digital-zoomed image of Fig. 3b with that of Fig. 3a, such bulges and the bright patches of Qdot labeling were found to be colocalized (arrowheads shown in the insets of Fig. 3a and b). Also, as shown in Fig. 3c, magnification of the boxed area in Fig. 3b showed the existence of small bumps at the corresponding locations of the bulges observed in Fig. 3b, as indicated by dotted circles. Although the exact mechanism of the aggregation of prestin in the plasma membrane of CHO cell is still unclear, these findings support the idea that prestin may be aggregated at focal adhesion sites at an early stage or even a late stage of cell adhesion. Thus, it is likely that prestin remains at the same location, possibly in an integrin-dependent manner. However, morphological and histological studies of prestin, other proteins related to the formation of focal adhesion and the plasma membrane of the CHO cells over time using AFM, electron microscopy, confocal laser scanning microscopy, and so on are needed to obtain more detailed information concerning this mechanism.

Prestin labeling with Qdot

To label prestin molecules in the plasma membranes of a prestin-transfected CHO cells with Qdots, in the present study, the plasma membranes were isolated and incubated with antiprestin antibody and Qdot-conjugated secondary antibody. Figure 4 shows high-magnification images of such membrane. Particles 8 nm in height, corresponding to Qdots, were clearly observed. Even after scanning the sample from the top to the bottom and subsequent scanning from the bottom to the top, the location of these particles

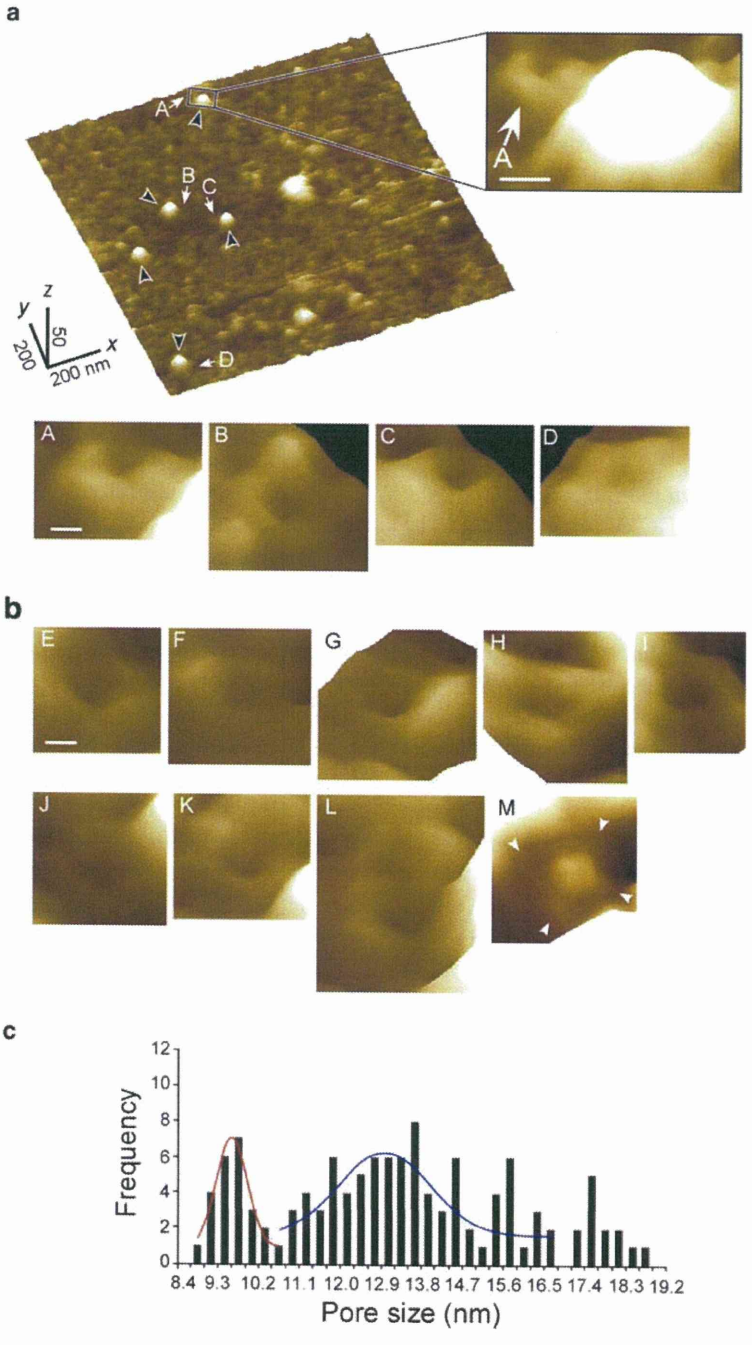

were unchanged, indicating that they were firmly attached to the isolated plasma membrane of the CHO cell. As a negative control, the plasma membrane was isolated from an untransfected CHO cell and subjected to the same sample preparation procedure. As shown in Fig. 5c, although there were a few accumulations more than 15 nm in height, probably the cytoskeletal materials and/or the peripheral proteins remained even after incubation with high-salt buffer and trypsin, no other obvious structures were seen, indicating that the Qdots did not exit.

To confirm whether the 8-nm particles observed on the isolated plasma membrane of the prestin-transfected CHO cell were Qdots, first, the size and shape of the Qdots used in the present study were measured on a mica substrate. Then, the size and shape of Qdots observed on the isolated plasma membranes were analyzed and compared with those

◀ **Fig. 8** Membrane topology of prestin on the cytoplasmic face of the plasma membrane of the prestin-transfected CHO cells. **a** High-magnification 3-D AFM images of the plasma membrane of the prestin-transfected CHO cell. Qdots 8 nm in height were clearly observed, as indicated by *black arrowheads*. As shown in the magnification at the *right*, a ring-like structure with four peaks and one valley at its center, possibly corresponding to a prestin molecule, was observed in the vicinity of the Qdot (*A*, *arrow*). Similar structures were observed at the location indicated by *arrows* (*A–D*), the magnifications of which are shown in the *bottom panels*. **b** Examples of 3-D images of the structures observed in the vicinity of the Qdots on the cytoplasmic faces of the isolated plasma membranes of the prestin-transfected CHO cells. These images were obtained from the different cells shown in **a**. Most of the observed structures are ring-like structures, each with a depression surrounded by four peaks (*E–K*). Such structures are sometimes adjacent to others, forming a unit with two molecules (*L*). Besides those ring-like structures, a square-shaped structure with a protrusion at its center, four corners of which are indicated by *arrowheads*, was also observed (*M*). The side length of the square, i.e., the length between the adjacent corners indicated by *arrowheads*, was 7.7 nm. The diameter of the protrusion was 6.2 nm. **c** Frequency distribution of the diameter of the ring-like structures (n=120) found around the Qdots (n=109) on the isolated plasma membranes of the prestin-transfected CHO cells (n=23). This histogram exhibited two main Gaussian distributions shown by *red* and *blue lines* (red, y_0=0.9±1.0, A=6.2±2.1, x_{width}=0.5±0.2; blue, y_0=1.6±0.7, A=4.6±1.2, x_{width}=1.4±0.5). The peaks of those distributions were 9.6±0.1 nm (*red*) and 13.0±0.2 nm (*blue*), respectively. Scale bars of the magnifications at the *right* and the *bottom* of **a** are 20 and 10 nm, respectively, and that of **b** is 10 nm

measured on mica. As shown in Fig. 6a, the Qdots were uniform-sized particle-like structures with a diameter of approximately 8 nm, which is in good agreement with a previously reported size of Qdots [28]. The sizes of the Qdots spread on mica showed a Gaussian distribution (red line, Fig. 6b), as did those on the isolated plasma membranes (blue line, Fig. 6b), although the distribution of the latter was much broader than that of the former. This difference may have been caused by the phospholipid membrane being relatively softer than the mica surface and/or by some materials attached to the surfaces of the Qdots and the plasma membrane, such as cell fragments and proteins contained in the culture medium, during the sample preparation. However, the average sizes of Qdots observed on the mica and the plasma membrane, i.e., 8.2±0.5 and 7.9±1.3 nm, respectively, were statistically identical (P>0.05, Student's t test; Fig. 6c), indicating that the particles 8 nm in height observed on the isolated plasma membrane of the prestin-transfected CHO cells were Qdots.

Although Qdots can be identified by checking their spherical shape and uniform size, in the present study, the existence of Qdots on the isolated plasma membrane of the CHO cell was further confirmed by using the phase imaging mode of AFM. The soft sample surface and/or the attractive interactions imposed on a tip of the AFM cantilever cause a negative phase shift, reflected as a dark phase contrast, whereas the stiff sample surface and/or the repulsive interaction between the tip and the sample cause a positive phase shift, reflected as a bright phase contrast [29]. Since the Qdots used in the present study were stiff semiconductor nanocrystals covered with soft antigoat IgG antibodies, the observed negative phase shift occurred at the peripheral part of the Qdot and the positive phase shift took place above the Qdot. Although several sizes of particles on the plasma membrane were observed in the height mode (A and B, Fig. 7a), only particle B, approximately 8 nm in height, showed a phase shift, that is, the bright phase contrast (positive phase shift) was observed at the center of the particle, whereas the dark phase contrast (negative phase shift) was observed at its periphery, suggesting that this particle was a Qdot.

Based on the two aspects mentioned above, the particles observed on the isolated plasma membranes of the prestin-transfected CHO cells were confirmed to be Qdots.

Membrane topology of prestin in the plasma membranes of CHO cells

In the present study, Qdots were used as topographic surface markers. Assuming the primary antibody binds at the tip of the N terminus and the secondary antibody conjugated with Qdot connects to the primary antibody, the maximum distance between a Qdot and a prestin molecule is estimated to be approximately 50 nm (see the "Analysis of AFM images" section). In the present study, all structures observed within 66.5 nm apart from the Qdot were subjected to the subsequent size analysis due to the architecture of the AFM system.

As shown in Fig. 8a, Qdots 8 nm in height were clearly observed on the cytoplasmic face of the isolated plasma membrane of the prestin-transfected CHO cell (black arrowheads). The magnification shown on the right revealed that a ring-like structure about 10 nm in diameter with four peaks and one valley at its center, possibly corresponding to a prestin molecule, existed in the vicinity of the Qdot. Such structures were also observed in the vicinity of Qdots indicated by the arrow (A–D, Fig. 8a), except for one Qdot, magnifications of which are shown in the bottom panels of Fig. 8a. Similarly shaped structures were also observed in the vicinity of Qdots on the cytoplasmic faces of the plasma membranes isolated from other prestin-transfected CHO cells (E–K, Fig. 8b). This configuration of prestin, i.e., four peaks at its periphery, suggests the tetrameric structure of prestin in the plasma membranes of prestin-transfected CHO cells. Sometimes, such structures are located adjacent to others (L, Fig. 8b), forming a unit with two (L, n=8), three (n=4), or four molecules (n=2). Although formation of such higher-order architectures were not frequent (approximately 14%), this

result implies that prestin molecules tend to be accumulated in the plasma membrane.

Besides the ring-like structures, a square-shaped structure with a protrusion at its center, four corners of which are indicated by arrowheads, was rarely observed (M, n=4). The side length of the square, i.e., the length between the adjacent corners indicated by arrowheads (M, Fig. 8b), and the diameter of the protrusion were 7.7 and 6.2 nm, respectively. This type of structure is quite similar to that reported by Mio et al. [12]. According to their report on TEM findings, prestin is a bullet-shaped particle with a small protrusion at its center which extends into the cytoplasm. In the present study, we isolated the inside-out plasma membranes of the prestin-transfected CHO cells and then imaged the cytoplasmic faces of such membranes. On this side, we observed ring-like structures, each with a depression at its center and four surrounding peaks, as shown in Fig. 8. The difference may be due to the difference in observation techniques, the main difference being the force applied to prestin molecules. In the present study, the sample was scanned by the cantilever, the spring constant of which was 0.02 N/m. During the scanning, as the distance between the tip of the cantilever and the sample was controlled so as to reduce the amplitude of the cantilever oscillation by approximately 2–5 nm during scanning, the force applied to the sample could be roughly estimated to be approximately 40–100 pN based on Hooke's law if the load applied to the sample is assumed to be static. In reality, however, since the cantilever was oscillated during scanning, this load was more likely dynamic, suggesting that the force applied to the sample was at least two times larger than such estimation. The application of such force to a protein has been reported to deform its structure [24, 30–32]. On the other hand, TEM does not load such force on the sample. Assuming the flexibility of the cytoplasmic protrusion of prestin, the possibility of deformation of this protrusion into its interior during AFM imaging cannot be ruled out.

In the present study, the topological data were continuously obtained in the transversal direction of the AFM image, i.e., left to right of the image along the x axis shown in Fig. 8a, while those in the transversal direction of the image, i.e., top to bottom of the image along the y axis, were intermittent, implying that the data obtained in the transversal direction were more reliable than those in the longitudinal direction. Therefore, all measured sizes were the transversal sizes of the observed structures. Analysis of sizes of the ring-like structures revealed that the frequency distribution of their diameter showed two main Gaussian distributions, the peaks of which were 9.6±0.1 and 13.0± 0.2 nm (shown by red and blue lines, respectively, in Fig. 8c). The sizes of the first and second peaks were consistent with the previously reported size of prestin [12, 14, 15, 17, 18], as shown in Table 1. If we assume that these two peaks correspond to the compact and extended states of prestin, the diameter change of prestin is approximately 3.4 nm. Based on this, the area change of prestin is calculated to be approximately 60.3 nm^2. In the previous study, the area change of prestin was assumed to be approximately 4 nm^2 [33]. This discrepancy probably relates to the diffusibility of prestin in the plasma membrane. The prestin molecules are considered to be diffusible in the lateral plasma membrane of OHCs [34–39]. In addition, in between the intramembrane molecules, including prestin, there are some spaces [13–18]. In such cases, a large extent of the area change in prestin should be dispersed in the plasma membrane, although to what degree the diffusibility and spaces between the molecules contribute to this dispersion is unknown. In such a scenario, the first peak is probably a smaller state of the ring-like structure and the second peak reflects its larger state, suggesting the existence of a compact as well as extended state of prestin.

As shown in Fig. 8c, the second peak showing the extended state of prestin is broader than the first peak showing its compact state. This result implies that the conformational change of prestin is not just a simple expansion change in sphere shape; rather, it is a directional change in the plane of the plasma membrane, e.g., from the compact sphere shape to the extended oval shape.

In the present study, prestin was observed to be a ring-like structure with a valley at its center surrounded by four

Table 1 Size of prestin

Sample	Method	Size (nm)	Reference
Freeze-fracture replica of the p-fracture face of the guinea pig OHC plasma membrane	SEM	10	Forge [14]
Freeze-fracture replica of the p-fracture face of the guinea pig OHC plasma membrane	SEM	11–15 (up to 20)	Kalinec et al. [15]
Cytoplasmic face of the guinea pig OHC plasma membrane	AFM	11–25	Grimellec et al. [17]
Cytoplasmic face of the gerbil prestin-transfected CHO cell plasma membrane	AFM	8–12	Murakoshi et al. [18]
Purified prestin obtained from rat prestin-transfected Sf9 cell membrane fraction	TEM	7.7–9.6	Mio et al. [12]
Cytoplasmic face of the gerbil prestin-transfected CHO cell plasma membrane	Immune AFM	9.6/13.0	This study

SEM scanning electron microscopy

peaks, suggesting a tetrameric structure of prestin. Analysis of the size of this structure demonstrated two peak distributions, implying the existence of the compact- and extended-state prestin. Utilizing the antibodies which label the C-terminal of prestin instead of those of prestin N-terminal used in this study would lead the important data on the oligomeric structure of prestin since the epitope of the C-terminal of prestin is probably exposed compared with that of the N-terminal [10] so that more precise information could be obtained from the immune AFM images. In addition, imaging with less force applied to the sample using a softer cantilever, appropriate chemical fixation of prestin molecules, and/or imaging the purified prestin molecules may contribute to further analysis of the detailed structure of prestin. Subjecting the isolated plasma membrane to a change in electric potential using a patch electrode or changing the composition of the buffer, e.g., increasing the concentration of Cl^- ions, could possibly yield further information about the mechanisms of the conformational change in prestin.

Conclusions

Prestin molecules expressed in the plasma membranes of prestin-transfected CHO cells were labeled with Qdots about 8 nm in height, which were clearly imaged by AFM. Ring-like structures, each with four peaks and one valley at its center, were observed in the vicinity of the Qdots, suggesting that these structures are prestin.

Acknowledgements This work was supported by Grant-in-Aid for Scientific Research on Priority Areas 15086202 from the Ministry of Education, Cultures, Sports, Science and Technology of Japan, Grant-in-Aid for Scientific Research (B) 18390455 from the Japan Society for the Promotion of Science, a Health and Labour Science Research Grant from the Ministry of Health, Labour and Welfare of Japan, Grant-in-Aid for Exploratory Research 18659495 from the Ministry of Education, Culture, Sports, Science and Technology of Japan, a grant from the Human Frontier Science Program, a grant from the Iketani Science and Technology Foundation and a grant from the Daiwa Securities Health Foundation to H.W., Grant-in-aid for JSPS Fellows 19002194 from the Japan Society for the Promotion of Science and Special Research Grants 11170012 and 11180001 from the Tohoku University 21st Century COE Program of the "Future Medical Engineering Based on Bio-nanotechnology" to M.M.

References

1. Brownell WE, Bader CR, Bertrand D, de Ribaupierre Y (1985) Evoked mechanical responses of isolated cochlear outer hair cells. Science 227:194–196
2. Kachar B, Brownell WE, Altschuler R, Fex J (1986) Electrokinetic shape changes of cochlear outer hair cells. Nature 322: 365–368
3. Ashmore JF (1987) A fast motile response in guinea-pig outer hair cells: the cellular basis of the cochlear amplifier. J Physiol 388:323–347
4. Santos-Sacchi J, Dilger JP (1988) Whole cell currents and mechanical responses of isolated outer hair cells. Hear Res 35:143–150
5. Dallos P, Fakler B (2002) Prestin, a new type of motor protein. Nat Rev Mol Cell Biol 3:104–111
6. Dallos P, Evans BN, Hallworth R (1991) Nature of the motor element in electrokinetic shape changes of cochlear outer hair cells. Nature 350:155–157
7. Zheng J, Shen W, He DZ, Long KB, Madison LD, Dallos P (2000) Prestin is the motor protein of cochlear outer hair cells. Nature 405:149–155
8. Zheng J, Long KB, Shen W, Madison LD, Dallos P (2001) Prestin topology: localization of protein epitopes in relation to the plasma membrane. NeuroReport 12:1929–1935
9. Deák L, Zheng J, Orem A, Du GG, Aguinaga S, Matsuda K, Dallos P (2005) Effects of cyclic nucleotides on the function of prestin. J Physiol 563:483–496
10. Navaratnam D, Bai JP, Samaranayake H, Santos-Sacchi J (2005) N-terminal-mediated homomultimerization of prestin, the outer hair cell motor protein. Biophys J 89:3345–3352
11. Zheng J, Du GG, Anderson CT, Keller JP, Orem A, Dallos P, Cheatham M (2006) Analysis of the oligomeric structure of the motor protein prestin. J Biol Chem 281:19916–19924
12. Mio K, Kubo Y, Ogura T, Yamamoto T, Arisaka F, Sato C (2008) The Motor Protein Prestin Is a Bullet-shaped Molecule with Inner Cavities. J Biol Chem 283:1137–1145
13. Arima T, Kuraoka A, Toriya R, Shibata Y, Uemura T (1991) Quick-freeze, deep-etch visualization of the 'cytoskeletal spring' of cochlear outer hair cells. Cell Tissue Res 263:91–97
14. Forge A (1991) Structural features of the lateral walls in mammalian cochlear outer hair cells. Cell Tissue Res 265:473–483
15. Kalinec F, Holley MC, Iwasa KH, Lim DJ, Kachar B (1992) A membrane-based force generation mechanism in auditory sensory cells. Proc Natl Acad Sci U S A 89:8671–8675
16. Souter M, Nevill G, Forge A (1995) Postnatal development of membrane specialisations of gerbil outer hair cells. Hear Res 91:43–62
17. Le Grimellec C, Giocondi MC, Lenoir M, Vater M, Sposito G, Pujol R (2002) High-resolution three-dimensional imaging of the lateral plasma membrane of cochlear outer hair cells by atomic force microscopy. J Comp Neurol 451:62–69
18. Murakoshi M, Gomi T, Iida K, Kumano S, Tsumoto K, Kumagai I, Ikeda K, Kobayashi T, Wada H (2006) Imaging by atomic force microscopy of the plasma membrane of prestin-transfected Chinese hamster ovary cells. J Assoc Res Otolaryngol 7:267–278
19. Iida K, Konno K, Oshima T, Tsumoto K, Ikeda K, Kumagai I, Kobayashi T, Wada H (2003) Stable expression of the motor protein prestin in Chinese hamster ovary cells. JSME Int J 46C:1266–1274
20. Iida K, Tsumoto K, Ikeda K, Kumagai I, Kobayashi T, Wada H (2005) Construction of an expression system for the motor protein prestin in Chinese hamster ovary cells. Hear Res 205:262–270
21. Murakoshi M, Wada H (2008) Atomic force microscopy in studies of the cochlea. In: Walker J (ed) Molecular protocols in auditory research. Humana Press, Totowa, NJ
22. Ziegler U, Vinckier A, Kernen P, Zeisel D, Biber J, Semenza G, Murer H, Groscurth P (1998) Preparation of basal cell membranes for scanning probe microscopy. FEBS Lett 436:179–184
23. Hartmann WK, Saptharishi N, Yang XY, Mitra G, Soman G (2004) Characterization and analysis of thermal denaturation of antibodies by size exclusion high-performance liquid chromatography with quadruple detection. Anal Biochem 325:227–239

24. Hertadi R, Gruswitz F, Silver L, Koide A, Koide S, Arakawa H, Ikai A (2003) Unfolding mechanics of multiple OspA substructures investigated with single molecule force spectroscopy. J Mol Biol 333:993–1002
25. Lärmer J, Schneider SW, Danker T, Schwab A, Oberleithner H (1997) Imaging excised apical plasma membrane patches of MDCK cells in physiological conditions with atomic force microscopy. Pflugers Arch 434:254–260
26. Iida K, Nagaoka T, Tsumoto K, Ikeda K, Kumagai I, Kobayashi T, Wada H (2004) Relationship between fluorescence intensity of GFP and the expression level of prestin in a prestin-expressing Chinese hamster ovary cell line. JSME Int J 47C: 970–976
27. Mitra K, Ubarretxena-Belandia I, Taguchi T, Warren G, Engelman DM (2004) Modulation of the bilayer thickness of exocytic pathway membranes by membrane proteins rather than cholesterol. Proc Natl Acad Sci U S A 101:4083–4088
28. Michalet X, Pinaud FF, Bentolila LA, Tsay JM, Doose S, Li JJ, Sundaresan G, Wu AM, Gambhir SS, Weiss S (2005) Quantum dots for live cells, in vivo imaging, and diagnostics. Science 307:538–544
29. Dong R, Yu LE (2003) Investigation of surface changes of nanoparticles using TM-AFM phase imaging. Environ Sci Technol 37:2813–2819
30. Janovjak H, Kedrov A, Cisneros DA, Sapra KT, Struckmeier J, Muller DJ (2006) Imaging and detecting molecular interactions of single transmembrane proteins. Neurobiol Aging 27:546–561
31. Dietz H, Bertz M, Schlierf M, Berkemeier F, Bornschlogl T, Junker JP, Rief M (2006) Cysteine engineering of polyproteins for single-molecule force spectroscopy. Nat Protoc 1:80–84
32. Cao Y, Li H (2008) How do chemical denaturants affect the mechanical folding and unfolding of proteins? J Mol Biol 375:316–324
33. Dong XX, Iwasa KH (2004) Tension sensitivity of prestin: comparison with the membrane motor in outer hair cells. Biophys J 86:1201–1208
34. Santos-Sacchi J (2002) Functional motor microdomains of the outer hair cell lateral membrane. Pflugers Arch 445:331–336
35. Zhang M, Kalinec F (2002) Structural microdomains in the lateral plasma membrane of cochlear outer hair cells. J Assoc Res Otolaryngol 3:289–301
36. Santos-Sacchi J, Zhao HB (2003) Excitation of fluorescent dyes inactivates the outer hair cell integral membrane motor protein prestin and betrays its lateral mobility. Pflugers Arch 446:617–622
37. de Monvel JB, Brownell WE, Ulfendahl M (2006) Lateral diffusion anisotropy and membrane lipid/skeleton interaction in outer hair cells. Biophys J 91:364–381
38. Organ LE, Raphael RM (2007) Application of fluorescence recovery after photobleaching to study prestin lateral mobility in the human embryonic kidney cell. J Biomed Opt 12:021003
39. Sturm AK, Rajagopalan L, Yoo D, Brownell WE, Pereira FA (2007) Functional expression and microdomain localization of prestin in cultured cells. Otolaryngol Head Neck Surg 136: 434–439

Neuroscience 164 (2009) 1312–1319

COCHLEAR OUTER HAIR CELLS IN A DOMINANT-NEGATIVE CONNEXIN26 MUTANT MOUSE PRESERVE NON-LINEAR CAPACITANCE IN SPITE OF IMPAIRED DISTORTION PRODUCT OTOACOUSTIC EMISSION

A. MINEKAWA,[a] T. ABE,[b] A. INOSHITA,[a] T. IIZUKA,[a] S. KAKEHATA,[b] Y. NARUI,[a] T. KOIKE,[c] K. KAMIYA,[a] H.-O. OKAMURA,[c] H. SHINKAWA[b] AND K. IKEDA[a]*

[a]*Department of Otorhinolaryngology, Juntendo University School of Medicine, Tokyo, Japan*

[b]*Department of Otorhinolaryngology, Hirosaki University School of Medicine, Hirosaki, Japan*

[c]*Department of Mechanical Engineering and Intelligent Systems, The University of Electro-Communications, Tokyo, Japan*

Abstract—Mutations in the connexin26 gene (GJB2) are the most common genetic cause of congenital bilateral non-syndromic sensorineural hearing loss. Transgenic mice were established carrying human Cx26 with the R75W mutation that was identified in a deaf family with autosomal dominant negative inheritance [Kudo T et al. (2003) Hum Mol Genet 12:995–1004]. A dominant-negative *Gjb2* R75W transgenic mouse model shows incomplete development of the cochlear supporting cells, resulting in profound deafness from birth [Inoshita A et al. (2008) Neuroscience 156:1039–1047]. The Cx26 defect in the *Gjb2* R75W transgenic mouse is restricted to the supporting cells; it is unclear why the auditory response is severely disturbed in spite of the presence of outer hair cells (OHCs). The present study was designed to evaluate developmental changes in the *in vivo* and *in vitro* function of the OHC, and the fine structure of the OHC and adjacent supporting cells in the R75W transgenic mouse. No detectable distortion product otoacoustic emissions were observed at any frequencies in R75W transgenic mice throughout development. A characteristic phenotype observed in these mice was the absence of the tunnel of Corti, Nuel's space, and spaces surrounding the OHC; the OHC were compressed and squeezed by the surrounding supporting cells. On the other hand, the OHC developed normally. Structural features of the lateral wall, such as the membrane-bound subsurface cisterna beneath the plasma membrane, were intact. Prestin, the voltage-dependent motor protein, was observed by immunohistochemistry in the OHC basolateral membranes of both transgenic and non-transgenic mice. No significant differences in electromotility of isolated OHCs during development was observed between transgenic and control mice. The present study indicates that normal development of the supporting cells is indispensable for proper cellular function of the OHC.

Key words: hereditary deafness, connexin26, *Gjb2*, outer hair cell, prestin, electromotility.

*Corresponding author. Tel: +81-3-5802-1229; fax: +81-3-5840-7103.
E-mail address: ike@juntendo.ac.jp (K. Ikeda).

Abbreviations: C_m, membrane capacitance; C_v, nonlinear capacitance; Cx26, connexin26; DAPI, 4′,6-diamidino-2-phenylindole; DPOAE, distortion product otoacoustic emission; GJB2, connexin26 gene; OHC, outer hair cell; P, postnatal day; PB, phosphate buffer; PBS, phosphate-buffered saline; PFA, paraformaldehyde.

The organ of Corti in mammals is a complex three-dimensional structure containing both sensory and supporting cells sitting on the basilar membrane. The supporting cells, including the pillar cells and Deiter's cells, form a rigid scaffold adjacent to and surrounding the outer hair cell (OHC) and confer essential mechanical properties for efficient transmission of stimulus-induced motion of the hair cells between the reticular lamina and the basilar membrane. Although development of pillar cells and the formation of a normal tunnel of Corti are required for normal hearing (Colvin et al., 1996), the physiological function of the supporting cells in postnatal development remains unclear.

Gap junction proteins in the cochlear supporting cells are believed to allow rapid removal of K^+ away from the base of hair cells, resulting in recycling back to the endolymph (Kikuchi et al., 1995). In addition to these effects on K^+, gap junction proteins act to mediate Ca^{2+} and anions such as inositol 1,4,5-trisphosphate, ATP, and cAMP as cell-signaling, nutrient, and energy molecules (Beltramello et al., 2005; Zhao et al., 2005; Piazza et al., 2007; Gossman and Zhao, 2008). In the developing postnatal cochlea, Tritsch et al. (2007) further found that within a transient structure known as Kolliker's organ, ATP can bind to P2X receptors on the inner hair cells, thus causing depolarization and Ca^{2+} influx, while also mimicking the effect of sound.

In the organ of Corti, most gap junctions are assembled from connexin (Cx) protein subunits, predominantly connexin 26 (Cx26, *Gjb2* gene) and co-localized Cx30 (Forge et al., 2003; Zhao and Yu, 2006). Mouse models have confirmed that Cx26 encoded by *Gjb2* is essential for cochlear function (Cohen-Salmon et al., 2002; Kudo et al., 2003). A dominant-negative *Gjb2* R75W transgenic mouse model shows incomplete development of the cochlear supporting cells, resulting in profound deafness from birth (Inoshita et al., 2008). Characteristic ultrastructural changes observed in the developing supporting cells of the *Gjb2* R75W transgenic mouse model include (i) the absence of the tunnel of Corti, Nuel's space, or spaces surrounding the OHCs; and (ii) reduced numbers of microtubules in the pillar cells. On the other hand, the development of the OHCs, at least from postnatal day 5 (P5) to P12 was not affected. The Cx26 defect in the *Gjb2* transgenic mouse is restricted to the supporting cells; it is thus difficult to explain why the auditory response is extensively disturbed despite the presence of the OHCs.

The present study was designed to evaluate developmental changes in the *in vivo* and *in vitro* function of the OHC together with the ultrastructure of the OHC and its adjacent

0306-4522/09 $ - see front matter
doi:10.1016/j.neuroscience.2009.08.043

supporting cells in the R75W transgenic mouse, to provide a better understanding of the functional properties of the supporting cells, and to gain new insights into the molecular and physiological mechanisms of *Gjb2*-based deafness.

EXPERIMENTAL PROCEDURES

Animals and anesthesia

All mice used for this study were obtained from a breeding colony of R75W transgenic mice (Kudo et al., 2003) and maintained at the Institute for Animal Reproduction (Ibaraki, Japan). R75W transgenic mice were maintained on a mixed C57BL/6 background and intercrossed to generate R75W transgenic animals. The animals were genotyped using DNA obtained from tail clips and amplified with the Tissue PCR Kit (Sigma, Saint Louis, MO, USA). The animals were deeply anesthetized with an intraperitoneal injection of ketamine (100 mg/kg, Ohara Pharamaceutical Co., Ltd., Tokyo, Japan) and xylazine (10 mg/kg) in all experiments. All experiment protocols were approved by the Institutional Animal Care and Use Committee at Juntendo University School of Medicine, and were conducted in accordance with the US National Institutes of Health Guidelines for the Care and Use of Laboratory Animals.

Distortion product otoacoustic emission

All electrophysiology was performed within an acoustically and electrically insulated and grounded test room. Distortion product otoacoustic emission (DPOAE) responses at 2f1–f2 were measured through the meatus using a measuring system (model ER-10B, Etymotic Research Inc., Elk Grove Village, IL, USA) with a probe developed for immature mice according to a previous paper (Narui et al., 2009). DPOAE stimuli were administered at two primary frequencies, f1 and f2, such that f1<f2. DPOAE input/output functions at f2=12, 30, and 45 kHz with f2/f1=1.2 were constructed. At each frequency pair, primary levels L1 (level of f1 tone) and L2 (level of f2 tone) were increased incrementally by 5 dB steps from 30 to 80 dB (f2=12 kHz and 30 kHz), and 30 to 70 dB (f2=45 kHz) with L1=L2. The DPOAE threshold level was defined as the dB level at which the 2f1–f2 distortion product was more than 10 dB above the noise level.

Non-linear capacitance

OHCs were obtained from acutely dissected organs of Corti from both transgenic and non-transgenic mice according to a previous report (Abe et al., 2007). Briefly, cochleae were dissected, and the organs of Corti were separated from the modiolus and stria vascularis. The organs were then digested with trypsin (1 mg/ml) in external solution (100 mM NaCl, 20 mM tetraethylammonium, 20 mM CsCl, 2 mM $CoCl_2$, 1.52 mM $MgCl_2$, 10 mM 4-(2-hydroxyethyl)-1-piperazineethanesulfonic acid and 5 mM dextrose (pH 7.2), 300 mosmol/L, in order to block ionic conductance) for 10–12 min at room temperature and transferred into 35 mm plastic dishes (Falcon, Lincoln Park, NJ, USA) with 2 ml external solution. OHCs were isolated by gentle trituration. The dish was mounted on an inverted microscope (IX71; Olympus, Tokyo, Japan).

The patch pipette solution contained 140 mM CsCl, 2 mM $MgCl_2$, 10 mM ethyleneglycoltetraacetic acid, 10 mM 4-(2-hydroxyethyl)-1-piperazineethanesulfonic acid (pH 7.2), 300 mosmol/L (adjusted with dextrose).

The cells were whole-cell voltage-clamped with an Axon (Burlingame, CA, USA) 200 B amplifier using patch pipettes having initial resistances of 3–5 MΩ. Series resistances, which ranged 5–20 MΩ, remained uncompensated for membrane capacitance (C_m) measurements, though corrections for series resistance voltage errors were made offline.

Data acquisition and analysis were performed using the Windows-based patch-clamp program jClamp (SciSoft, New Haven, CT, USA).

The C_m functions were obtained 1 min after establishment of the whole-cell configuration. C_m was assessed using a continuous high-resolution (2.56 ms sampling) two-sine voltage stimulus protocol (10 mV peak at both 390.6 and 781.2 Hz) superimposed onto a voltage ramp (200 ms duration) from −150 to +150 mV (Santos-Sacchi et al., 1998; Santos-Sacchi, 2004). The capacitance data were fit to the first derivative of a two-state Boltzmann function (Santos-Sacchi, 1991).

$$C_m = Q_{max}\frac{ze}{kT}\frac{b}{(1+b)^2} + C_{lin}$$

$$b = \exp\left(\frac{-ze(V_m - V_{pkcm})}{kT}\right)$$

where Q_{max} is the maximum nonlinear charge moved, V_{pkcm} is voltage at peak capacitance or half-maximum charge transfer, V_m is membrane potential, z is valence, C_{lin} is linear membrane capacitance, e is electron charge, k is Boltzmann's constant, and T is absolute temperature. For analyses, we quantified C_v, peak, an estimate of maximum voltage-dependent, nonlinear capacitance, as the absolute peak capacitance minus linear capacitance.

Histology

The mice were perfused with 4.0% paraformaldehyde (PFA) and 2.0% glutalaldehyde (pH 7.4) in 0.1 M phosphate buffer (PB). The inner ears were dissected and immersed in fixative overnight at room temperature. Decalcification was completed by immersion in 0.12 M ethylenediaminetetraacetic acid with gentle stirring at room temperature for a day. The cochleas were flushed again with buffer prior to perfusion with a warm solution of 10% gelatin. They were chilled on ice, thus allowing the gelatin to solidify, and then cut in half under a dissecting microscope. The half cochleas were rinsed (four times for 1 min each) with warm PB (40 °C) to remove residual gelatin. The specimens were post-fixed 1.5 h in 2.0% OsO_4 in 0.1 M PB, then dehydrated through graded ethanols and embedded in Epon. Semithin sections (1 μm) were stained with Toluidine Blue for light microscopy. Ultrathin sections were stained with uranyl acetate and lead citrate and examined by electron microscopy (HITACHI H7100, Japan).

Immunohistochemistry

The cochleae were removed after cardiac perfusion with 4% PFA (pH 7.4), placed in the same fixative at room temperature for 1 h, decalcified with 0.12 M ethylenediaminetetraacetic acid (pH 7.0) at 4 °C overnight. The specimens were dehydrated through graded concentrations of alcohol, embedded in paraffin blocks and sectioned into 5 μm thick slices. The sections were washed in several changes of 0.01 M phosphate-buffered saline (PBS; pH 7.2), blocked with 2% bovine serum albumin in 0.01 M PBS for 30 min, and then were incubated for 1 h at room temperature with goat polyclonal antibodies to Prestin (1:100; Santa Cruz Biotechnology, Santa Cruz, CA, USA) (Kitsunai et al., 2007) diluted in 0.01 M PBS+1% bovine serum albumin. The following day, the tissues were rinsed with 0.01 M PBS, incubated for 1 h at room temperature with a Alexa-Fluor-594 conjugated donkey anti-goat (1:1000; Molecular Probes, Eugene, OR, USA), rinsed with 0.01 M PBS, and then mounted in Vectashield containing DAPI (Vector Laboratories, Burlingame, CA, USA). Labeling was viewed using a confocal laser scanning microscope (LSM510 META, Carl Zeiss, Esslingen, Germany), and each image was analyzed and saved using the ZeissLSM image Browzer (Carl Zeiss).

Statistical analysis

Data were expressed as mean±SEM. Input/output function data of the amplitudes were analyzed via a non-repeated measures analysis of variance (ANOVA). The significance of DPOAE amplitudes was analyzed further by post hoc multiple comparison tests using the Bonferroni procedure. The statistical difference of DPOAE threshold was determined by a two-sided Mann–Whitney's *U*-test. $P<0.05$ was accepted as the level of significance.

RESULTS

Distortion product otoacoustic emission

DPOAE responses were examined during postnatal development. Non-transgenic mice started to show a measurable response of DPOAE from P12–14 followed by gradual increase of amplitude (Fig. 1A, B, C). Significant differ-

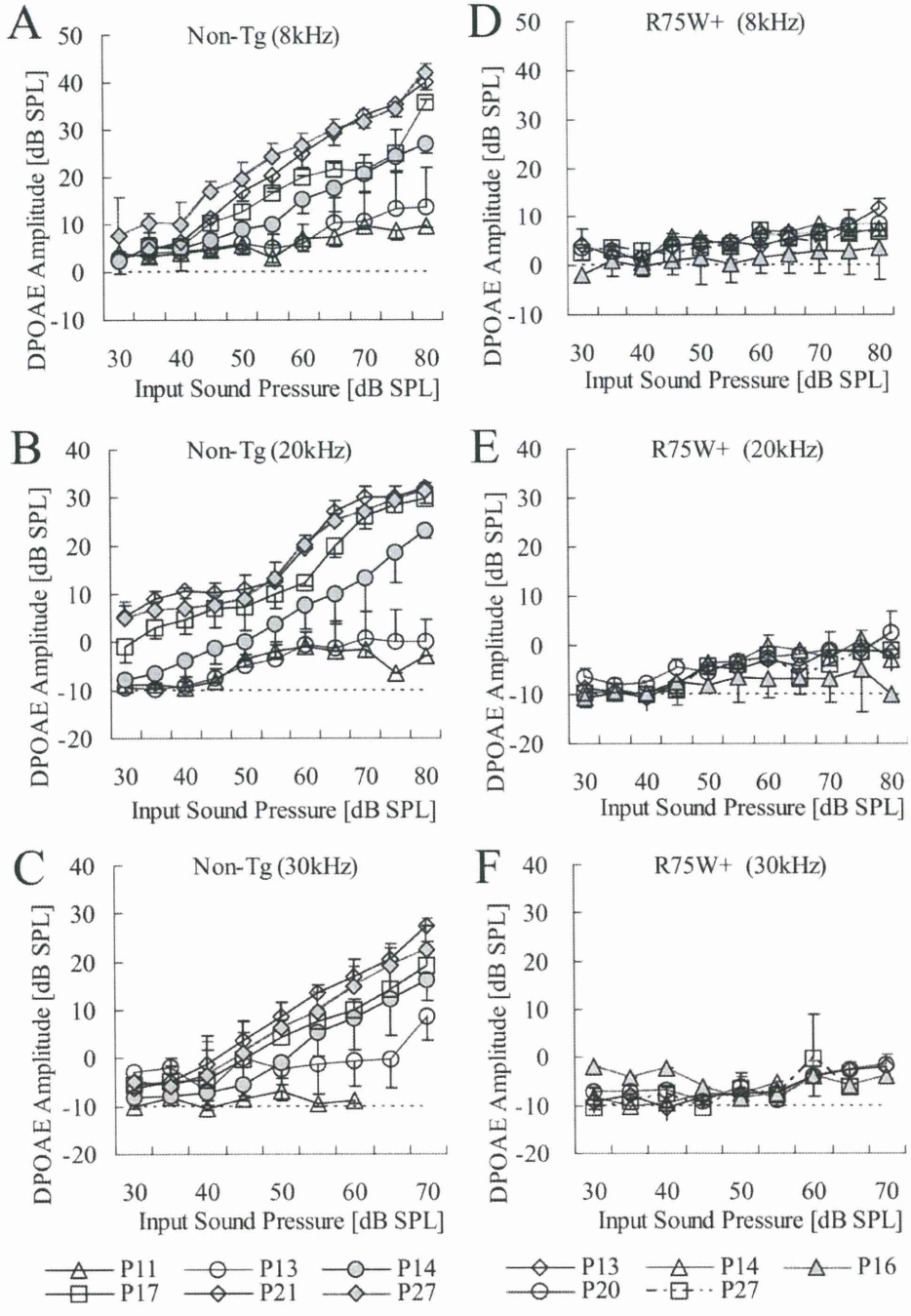

Fig. 1. Input/output function of the amplitudes of non-transgenic (A, B, C) and R75W transgenic (D, E, F) mice at 8 kHz, 20 kHz and 30 kHz frequencies (2f1–f2) from P11 to P27. DPOAE data were plotted as mean±SEM. The dotted line is the noise level. Non-Tg: non-transgenic mice, R75W+: R75W transgenic mice.

ences of the DPOAE amplitudes of the non-transgenic mice in comparison to noise levels appeared at P12–14 for the different stimuli tested. In contrast, there were no statistically significant differences between noise level and DPOAE amplitudes at 8 kHz, 20 kHz, and 30 kHz throughout postnatal development in the R75W transgenic mice. Furthermore, no DPOAE was detected at any frequencies in R75W transgenic mice throughout postnatal development (Fig. 1D, E, F).

The mean DPOAE thresholds of non-transgenic mice were abruptly reduced around P13–P14 to reach the adult level by P16. In contrast, the mean DOPAE thresholds of R75W transgenic mice stayed at high level throughout postnatal development (Fig. 2).

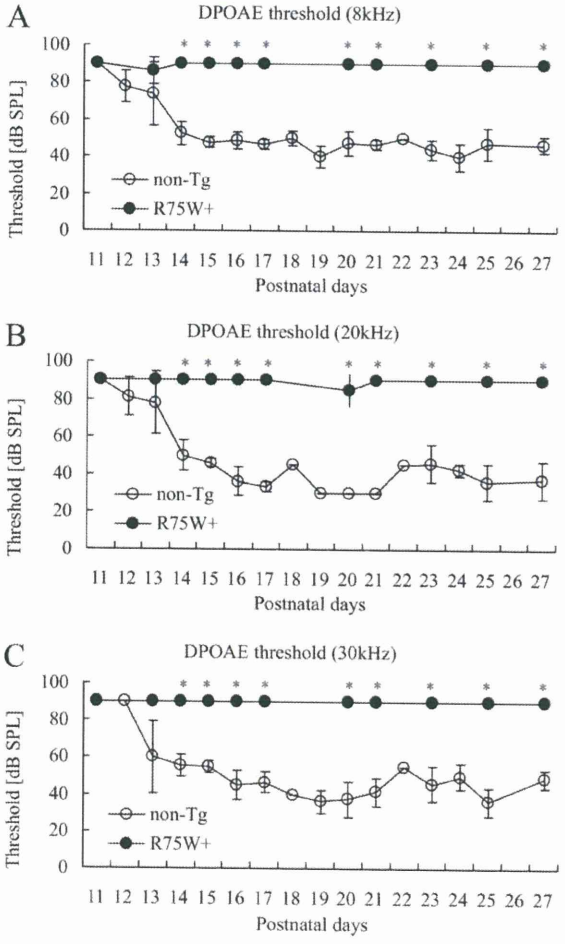

Fig. 2. DPOAE thresholds at 8 kHz (A), 20 kHz (B), and 30 kHz (C) frequencies of non-transgenic mice (open circle) and R75W transgenic mice (filled circle) from P11 to P27. The DPOAE threshold level was defined as the dB level at which the 2f1–f2 distortion product was more than 10 dB above the noise level. In the case of no DPOAE, the threshold level was defined as 90 dB. *: Significant difference between non-transgenic and transgenic mice ($P<0.05$). Non-Tg: non-transgenic mice, R75W+: R75W transgenic mice.

Histology and immunohistochemistry

The cytoarchitecture of the organ of Corti of the R75W transgenic mouse was remarkably different from that of the non-transgenic mouse (Fig. 3A, B). Transverse sections of the organ of Corti in R75W transgenic mouse revealed compression and squeezing of the OHC by the surrounding supporting cells, and Nuel's space around each OHC was occupied by Deiter's cells (Fig. 3B). Structural changes in the OHCs and adjacent cells are likely to restrict the electrically-induced motility of the OHC. The mesothelial cells associated with the basilar membrane in the transgenic mouse were cuboidal and more densely packed in contrast to a flattened layer in the control mouse. However, the ultrastructure of the OHCs in the non-transgenic mouse was comparable to that of the R75W transgenic mouse (Fig. 3C, D). The OHC of both mice showed consistent characteristic features; (i) a relatively high proportion of cytoplasm having a basally located nucleus, (ii) a smooth plasma membrane lined by a thick layer of subsurface cisternae, (iii) numerous mitochondria along the lateral membrane, and (iv) no vacuole formation in the cytoplasm and no condensation of chromatin in the nucleus.

Immunofluorescence microscopy of cross-cochlear sections was used to examine the distribution of prestin in the apical turns of the cochlea of non-transgenic and R75W transgenic mice at P12. Prestin labeling was clearly visible on the whole OHC basolateral wall in both the control (Fig. 4A) and R75W+ mice (Fig. 4B) at P12. On the other hand, the nucleus and the cuticular plate of both mice were devoid of immunostaining.

These ultrastructural and immunohistochemical results support the notion that the OHC are equipped with the morphological and molecular bases to produce electromotility.

Electromotility of OHCs

The signature electrical response of an adult OHC is a bell-shaped, voltage-dependent capacitance, which represents the conformational fluctuations of the motor molecule. In wild-type of C57BL/6J mice, *Cv* increased rapidly during development, saturating at P18 (Abe et al., 2007). OHCs from both R75W transgenic and non-transgenic mice showed somatic shape change in response to the voltage change (data not shown) and showed a typical bell-shaped voltage dependence (Fig. 5A). *Cv* increased progressively from P9 and saturated at P24. The time course of *Cv* in R75W transgenic and non-transgenic mice showed no significant difference (Fig. 5B). These results indicate that the development of OHC motility is not affected in R75W transgenic mice.

DISCUSSION

The present study demonstrated that a dominant-negative R75W mutation of *Gjb2* failed to generate a detectable DPOAE from birth in spite of the presence of OHCs and apparently normal electromotility. The DPOAE depends on two factors, an intact OHC system (Long and Tubis, 1988; Brown et al., 1989) and a positive endocochlear potential

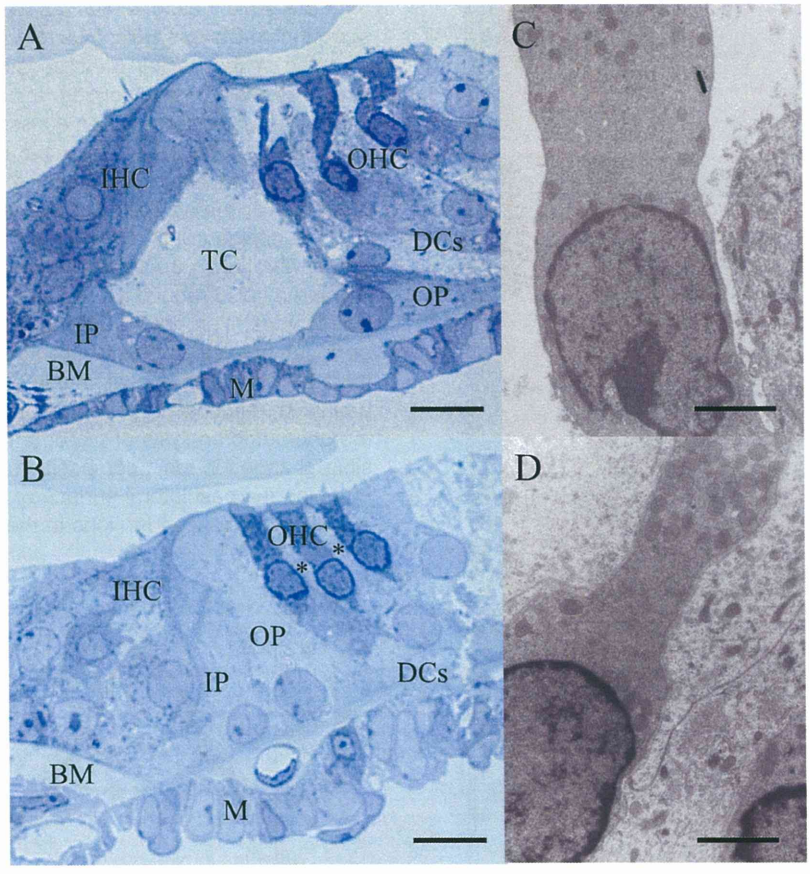

Fig. 3. Histology and transmission electron micrographs of non-transgenic (A, C) and R75W transgenic (B, D) mice. At P12, tunnel of Corti is detected in non-transgenic mice (A), but not (asterisk) in R75W transgenic mice (B). Nuel's space is formed in non-transgenic mice (A, C), but not in R75W transgenic mice (B, D). OHCs are detected in both non-transgenic (A) and R75W transgenic mice, but are squeezed by the surrounding Deiter's in R75W transgenic mice (B). The OHCs showed normal development, with preserved fine structure of the lateral wall, membrane-bound subsurface cisterna beneath the plasma membrane, and enriched mitochondria in both the non-transgenic (C) and R75W transgenic mice (D). Scale bars are 10 μm (A, B) and 2 μm (C, D). Abbreviations used: TC, tunnel of Corti; IP, inner pillar cell; OP, outer pillar cell; BM, basilar membrane; M, mesothelial cell.

(Brownell, 1990). The R75W transgenic mice have a normal endocochlear potential (Kudo et al., 2003). Furthermore, the OHC develops normally with apparently intact fine structure of the lateral wall, including normal membrane-bound subsurface cisterna beneath the plasma membrane. The characteristic phenotype observed in the R75W transgenic mice was the absence of the tunnel of Corti, Nuel's space, and spaces surrounding the OHC, related to abnormal development of the supporting cells.

The mammalian cochlea uses a unique mechanism for amplification of sound signals. Cochlear amplification is thought to originate from (1) somatic motility based on the cochlear motor prestin and (2) hair cell bundle motor related to mechanoelectrical channel (Robles and Ruggero, 2002). Distortion and cochlear amplification are believed to stem from a common mechanism. A recent study (Verpy et al., 2008) postulated that the main source of cochlear waveform distortions is a deflection-dependent hair bundle stiffness derived from stereocilin associated with the horizontal top connectors. However, the relationship between stereocilin and prestin is still unclear.

Somatic electromotility of the OHC is a voltage-dependent rapid alteration of OHC length and stiffness. The electromotility of the OHC is thought to amplify the motion of the basilar membrane at low sound pressure levels and compress it at high levels (Patuzzi et al., 1989; Ruggero and Rich, 1991; Kossl and Russell, 1992). Prestin, which resides in the basolateral membrane of the cochlear OHC (Yu et al., 2006), acts as a voltage-dependent motor protein responsible for OHC electromotility (Belyantseva et al., 2000; Zheng et al., 2000; Liberman et al., 2002). The present study demonstrated that the voltage-dependent, nonlinear capacitance representing the conformational fluctuations of the motor molecule progressively increased from P10 to P18 in *Gjb2* R75W transgenic mice. The developmental changes in the OHC electromotility observed in the *Gjb2* R75W transgenic mice resemble those of both the C57BL/6J mouse in a previous study (Abe et al., 2007) and the littermate non-transgenic mice in the present study.

At least three factors that could explain the discrepancy between the DPOAE and the OHC electromotility

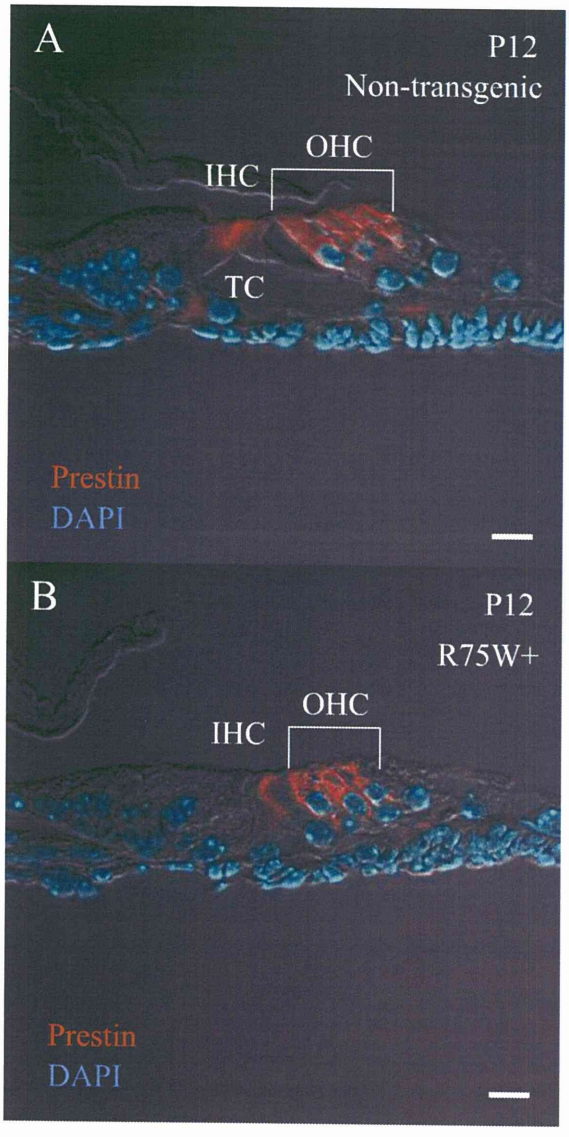

Fig. 4. A cross-sectional immunofluorescent analysis of prestin distributed in the apical turns of the cochlea of non-transgenic (A) and R75W transgenic mice (B) at P12. Prestin labeling (red) is clearly visible on the whole OHC basolateral wall in both the non-transgenic (A) and R75W transgenic mice (B) at P12. The extracellular space around the OHC in R75W transgenic mice is narrower than that in non-transgenic mice. On the other hand, the nucleus stained with DAPI (blue) and the cuticular plate of both mice are devoid of immunostaining. Abbreviations used: OHC, outer hair cell; IHC, inner hair cell. Scale bars are 10 μm (A, B).

arising from the failure of development of the supporting cells can be proposed. First, mature OHCs are supported by underlying Deiter's cells, flanked on the lateral edge by a several rows of Hensen's cells, and anchored by the reticular lamina at their apical surface. The three-dimensional structure of the OHCs enable the longitudinal changes driven by transmembrane potential changes. In the transgenic mouse, the OHCs were compressed by the surrounding Deiter's cells, thus restricting motility. Second, vibration of the basilar membrane may be related to its thickness, which would contribute to the sensitivity and the production of the otoacoustic emissions (Kossl and Vater, 1985) and further to the tonotopic changes of the developing gerbil cochlea (Schweitzer et al., 1996). The thickened basilar membrane observed in the transgenic mice might suppress the DPOAE by reducing the basilar membrane vibration. Structural changes in the basilar membrane may also reduce the sound-induced vibration of the cochlear partition, thus inhibiting deflection of stereocilia on inner hair cells. This could explain why *Gjb2* R75W transgenic mice show remarkable elevation of the auditory brainstem response threshold (Inoshita et al., 2008). Third, morphometric analysis of the organ of Corti suggest possible changes in ionic composition of the cortilymph surrounding the basolateral surface of the OHCs (Inoshita et al., 2008). Increased K^+ ions in the cortilymph would de-

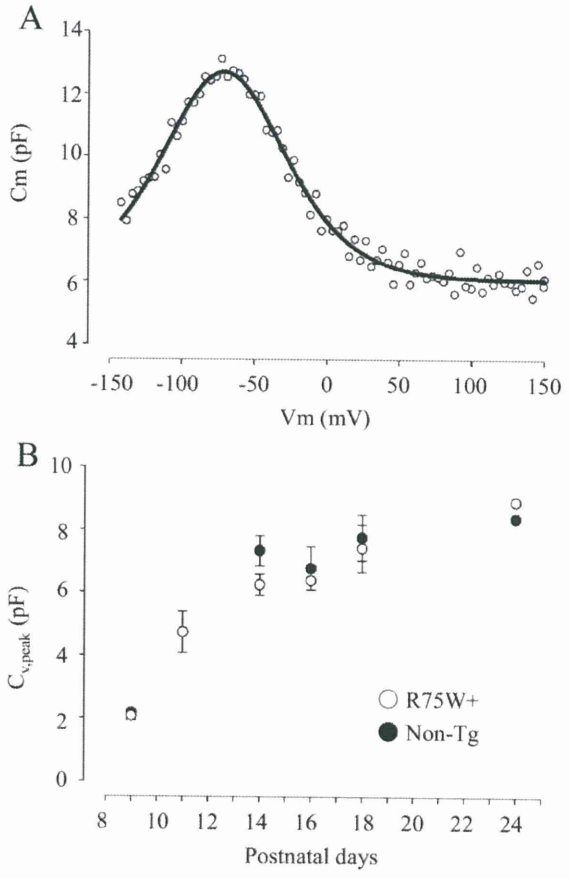

Fig. 5. Electrical responses of isolated OHC. C_m is expressed as a function of V_m at P14 in the R75W transgenic mouse (A). Fitted parameters are Q_{max}=0.704 pC, z=0.89. C_v, peak is expressed as a function of postnatal day (B). The number of cells in non-transgenic (closed circle) and R75W transgenic mice (open circle) was (from P9 to P24) 1–2, 0–3, 2–3, 5–2, 3–3, and 1–1, respectively. Standard error is plotted. Non-Tg: non-transgenic mice, R75W+: R75W transgenic mice.

polarize the OHCs, and decreased driving force across the mechanosensitive channels could affect OHC electromotility. The progressive degeneration of OHCs observed in the adult R75W transgenic mice (Kudo et al., 2003) may be brought about by disturbed homeostasis of the cortilymph.

The secondary hair cell loss in adult R75W transgenic mice (Kudo et al., 2003; Inoshita et al., 2008) implies that the restoration of hearing requires the regeneration of hair cells in addition to introduction of the *Gjb2* gene. The present study clearly showed both morphological and functional maturation of OHC until late in development, suggesting that a dominant-negative R75W mutation of *Gjb2* does not affect the genes that determine or control the differentiation of the OHC. Therefore, gene transfer of *Gjb2* into the supporting cells before hair cell degeneration could be used to treat deafness. Transgene expression has been accomplished in the supporting cells of the neonatal mouse cochlea using adeno-associated viral vectors without causing additional damage to the cochlea (Iizuka et al., 2008). Therefore, the present study provides a new strategy to restore hearing in *Gjb2*-based mutation.

CONCLUSION

OHC from the dominant-negative R75W mutation of *Gjb2* showed normal development and maturation, and isolated OHC clearly showed voltage-dependent, nonlinear capacitance with characteristic subcellular features. However, the DPOAE, which serves as an index for *in vivo* cochlear amplification, was remarkably suppressed in the mutant mice. This may result from disturbed development of the supporting cells surrounding the OHCs. The present study confirmed that the normal development of the supporting cells is indispensable for the cellular function of the OHC.

REFERENCES

Abe T, Kakehata S, Kitani R, Maruya S, Navaratnam D, Santos-Sacchi J, Shinkawa H (2007) Developmental expression of the outer hair cell motor prestin in the mouse. J Membr Biol 215:49–56.

Beltramello M, Piazza V, Bukauskas FF, Pozzan T, Mammano F (2005) Impaired permeability to Ins(1,4,5)P3 in a mutant connexin underlies recessive hereditary deafness. Nat Cell Biol 7: 63–69.

Belyantseva IA, Adler HJ, Curi R, Frolenkov GI, Kachar B (2000) Expression and localization of prestin and the sugar transporter GLUT-5 during development of electromotility in cochlear outer hair cells. J Neurosci 20:RC116.

Brown AM, McDowell B, Forge A (1989) Acoustic distortion products can be used to monitor the effects of chronic gentamicin treatment. Hear Res 42:143–156.

Brownell WE (1990) Outer hair cell electromotility and otoacoustic emissions. Ear Hear 11:82–92.

Cohen-Salmon M, Ott T, Michel V, Hardelin JP, Perfettini I, Eybalin M, Wu T, Marcus DC, Wangemann P, Willecke K, Petit C (2002) Targeted ablation of connexin26 in the inner ear epithelial gap junction network causes hearing impairment and cell death. Curr Biol 12:1106–1111.

Colvin JS, Bohne BA, Harding GW, McEwen DG, Ornitz DM (1996) Skeletal overgrowth and deafness in mice lacking fibroblast growth factor receptor 3. Nat Genet 12:390–397.

Forge A, Becker D, Casalotti S, Edwards J, Marziano N, Nevill G (2003) Gap junctions in the inner ear: comparison of distribution patterns in different vertebrates and assessement of connexin composition in mammals. J Comp Neurol 467:207–231.

Gossman DG, Zhao HB (2008) Hemichannel-mediated inositol 1,4,5-trisphosphate (IP3) release in the cochlea: a novel mechanism of IP3 intercellular signaling. Cell Commun Adhes 15: 305–315.

Iizuka T, Kanzaki S, Mochizuki H, Inoshita A, Narui Y, Furukawa M, Kusunoki T, Saji M, Ogawa K, Ikeda K (2008) Noninvasive in vivo delivery of transgene via adeno-associated virus into supporting cells of the neonatal mouse cochlea. Hum Gene Ther 19:384–390.

Inoshita A, Iizuka T, Okamura HO, Minekawa A, Kojima K, Furukawa M, Kusunoki T, Ikeda K (2008) Postnatal development of the organ of Corti in dominant-negative Gjb2 transgenic mice. Neuroscience 156:1039–1047.

Kikuchi T, Kimura RS, Paul DL, Adams JC (1995) Gap junctions in the rat cochlea: immunohistochemical and ultrastructural analysis. Anat Embryol (Berl) 191:101–118.

Kitsunai Y, Yoshida N, Murakoshi M, Iida K, Kumano S, Kobayashi T, Wada H (2007) Effects of heat stress on filamentous actin and prestin of outer hair cells in mice. Brain Res 1177:47–58.

Kossl M, Russell IJ (1992) The phase and magnitude of hair cell receptor potentials and frequency tuning in the guinea pig cochlea. J Neurosci 12:1575–1586.

Kossl M, Vater M (1985) Evoked acoustic emissions and cochlear microphonics in the mustache bat, Pteronotus parnellii. Hear Res 19:157–170.

Kudo T, Kure S, Ikeda K, Xia AP, Katori Y, Suzuki M, Kojima K, Ichinohe A, Suzuki Y, Aoki Y, Kobayashi T, Matsubara Y (2003) Transgenic expression of a dominant-negative connexin26 causes degeneration of the organ of Corti and non-syndromic deafness. Hum Mol Genet 12:995–1004.

Liberman MC, Gao J, He DZ, Wu X, Jia S, Zuo J (2002) Pressing is required for electromotility of the outer hair cell and for the cochlear amplifier. Nature 419:300–304.

Long GR, Tubis A (1988) Investigations into the nature of the association between threshold microstructure and otoacoustic emissions. Hear Res 36:125–138.

Narui Y, Minekawa A, Iizuka T, Furukawa M, Kusunoki T, Koike T, Ikeda K (2009) Development of distortion product otoacoustic emissions in C57BL/6J mice. Int J Audiol 48:576–581.

Patuzzi RB, Yates GK, Johnstone BM (1989) Outer hair cell receptor current and sensorineural hearing loss. Hear Res 42:47–72.

Piazza V, Ciubotaru CD, Gale JE, Mammano F (2007) Purinergic signalling and intercellular Ca2+ wave propagation in the organ of Corti. Cell Calcium 41:77–86.

Robles L, Ruggero MA (2002) Mechanics of the mammalian cochlea. Physiol Rev 81:1305–1352.

Ruggero MA, Rich NC (1991) Furosemide alters organ of corti mechanics: evidence for feedback of outer hair cells upon the basilar membrane. J Neurosci 11:1057–1067.

Santos-Sacchi J (1991) Reversible inhibition of voltage-dependent outer hair cell motility and capacitance. J Neurosci 11:3096–3110.

Santos-Sacchi J (2004) Determination of cell capacitance using the exact empirical solution of partial differential Y/partial differential Cm and its phase angle. Biophys J 87:714–727.

Santos-Sacchi J, Kakehata S, Takahashi S (1998) Effects of membrane potential on the voltage dependence of motility-related charge in outer hair cells of the guinea-pig. J Physiol 510: 225–235.

Schweitzer L, Lutz C, Hobbs M, Weaver SP (1996) Anatomical correlates of the passive properties underlying the developmental shift in the frequency map of the mammalian cochlea. Hear Res 97:84–94.

Tritsch NX, Yi E, Gale JE, Glowatzki E, Bergles DE (2007) The origin of spontaneous activity in the developing auditory system. Nature 450:50–55.

Verpy E, Weil D, Leibovici M, Goodyear RJ, Hamard G, Houdon C, Lefèvre GM, Hardelin JP, Richardson GP, Avan P, Petit C (2008) Stereocilin-deficient mice reveal the origin of cochlear waveform distortions. Nature 456:255–258.

Yu N, Zhu ML, Zhao HB (2006) Prestin is expressed on the whole outer hair cell basolateral surface. Brain Res 1095:51–58.

Zhao HB, Yu N, Fleming CR (2005) Gap junctional hemichannel-mediated ATP release and hearing controls in the inner ear. Proc Natl Acad Sci U S A 102:18724–18729.

Zhao HB, Yu N (2006) Distinct and gradient distributions of connexin26 and connexin30 in the cochlear sensory epithelium of guinea pigs. J Comp Neurol 499:506–518.

Zheng J, Shen W, He DZ, Long KB, Madison LD, Dallos P (2000) Prestin is the motor protein of cochlear outer hair cells. Nature 405:149–155.

(Accepted 19 August 2009)
(Available online 25 August 2009)

informa
healthcare

Original Article

International Journal of Audiology 2009; 48:576–581

*Yuya Narui**
*Akira Minekawa**
*Takashi Iizuka**
*Masayuki Furukawa**
*Takeshi Kusunoki**
Takuji Koike[§]
*Katsuhisa Ikeda**

*Department of Otorhinolaryngology, Juntendo University School of Medicine, Tokyo, Japan
[§]Department of Mechanical Engineering and Intelligent Systems, The University of Electro-Communications, Tokyo, Japan

Key Words
Development
Mouse
Distortion product otoacoustic emission
Auditory brainstem response

Abbreviations
ABR: Auditory brainstem response
DPOE: Distortion product otoacoustic emission

Development of distortion product otoacoustic emissions in C57BL/6J mice

Abstract
Distortion product otoacoustic emissions (DPOAEs) have been used to examine the development of hearing in the rat and gerbil. However, no reports of DPOAE measurement from the onset of hearing in mice are available. Commercially-available components were assembled and adapted to provide a suitable probe microphone and sound delivery system for measuring DPOAE in developing C57BL/6J mice. Furthermore, DPOAE data were compared with the findings of the auditory brainstem response (ABR). DPOAEs were obtained at 8 kHz from 11 days after birth, 20 kHz from 12 days, and 30 kHz from 13 days. Adult-like patterns of DPOAE were obtained 21 days at 8 and 20 kHz, and 28 days at 30 kHz. On the other hand, the ABR thresholds at 12 to 36 kHz appeared between 11 and 12 days and were saturated at 14 days. Based on these data, the onset of measureable DPOAEs in the mouse were earlier than in the rat and gerbil. The maturation of DPOAE in the mouse begins at a lower frequency in the high frequency range. In addition, the ABR threshold reached maturation earlier than DPOAE.

Sumario
Las emisiones otoacústicas por productos de distorsión de las emisiones otoacústicas (DPOAE) han sido utilizados para examinar el desarrollo de la audición en las ratas y los jerbos. Sin embargo, no hay mediciones disponibles de los DPOAE del inicio de la audición en ratones. Se ensamblaron y adaptaron partes de componentes disponibles comercialmente para lograr una sonda con micrófono y un sistema de sonido para la medición de DPOAE en ratones C57BL/6J en desarrollo. Incluso los datos de los DPOAE fueron comparados con los hallazgos de los potenciales evocados de tallo cerebral (ABR). Se obtuvieron DPOAE a 8 kHz, 11 días después del nacimiento, a 20 kHz a los 12 días y a 30 kHz a los 13 días. Se obtuvieron patrones de DPOAE parecidos a los de los adultos a los 21 días en 8 y 20 kHz y a los 28 días a 30 kHz. Por otro lado, los umbrales de los ABR de 12 a 36 kHz aparecieron entre 11 y 12 días y fueron saturados a los 14 días. Con base en estos datos la aparición de DPOAE medibles en estos ratones son más tempranos que en la rata y el jerbo. La maduración de los DPOAE en los ratones comienza en una frecuencia más baja en el rango de frecuencias altas. Además los umbrales de ABR alcanzan su madurez antes que los DPOAE.

The auditory function has been extensively studied in various mammals using several methods. The auditory brainstem response (ABR) has emerged as the most commonly used tool in the assessment of auditory function during development. The non-invasive character and simplicity of ABR recording has made it the tool of choice in this application. Another noninvasive tool used to assess auditory function is measurement of the distortion product otoacoustic emission (DPOAE) which is a type of cochlea-generated signal for evaluating the status of the outer hair cells in an intact endocochlear potential (Brownell, 1990). These acoustic signals, which can be recorded in the external ear canal, are generated within the cochlea in response to simultaneous stimulation of the same ear by two different frequency tones (Probst et al, 1991). DPOAEs are very sensitive to aging, noise exposure, and drug toxicity (Henley & Rybak, 1995; Parham, 1997; Mills & Rubel, 1994; Mills, 2003), and provide noninvasive probes for evaluating the cochlear functioning.

The DPOAE measurements have been used to examine the development of stimulus transduction along the basilar membrane in the rat and gerbil (Lenoir & Puel, 1987; Henley et al, 1990; Norton et al, 1991; Mills & Rubel, 1996). The fact that emissions provide frequency-specific information makes them especially attractive for such investigations. DPOAEs have been found to be reliably measureable in neonatal gerbils (Mills & Rubel, 1996; Mills, 2004) and rats (Lenoir & Puel, 1987; Henley et al, 1990). Several investigators also (Li et al, 1999; Varghese et al, 2005; Inagaki et al, 2006; Noguchi et al, 2006; Zhu et al, 2007) have focused on DPOAEs in young mice, namely at 4 to 6 weeks of age. Recently, the mouse has been used as an animal model for various hearing disorders. It is useful to measure auditory function throughout the life of the mouse in studies such as those directed toward genetic disorders (for example, see Minowa et al, 1999; Kudo et al, 2003). However, postnatal development of DPOAEs from the onset of hearing in mice has not been reported.

A mouse is smaller than a gerbil, so it possesses a narrower external auditory canal than a gerbil and extremely high frequency hearing. Namely, in the measurement of high frequency sound, the wavelength is too short to avoid the resonance of both the external auditory meatus and the inner space of the conventional probe used for DPOAE measurements. Resonance prevents the correct measurement of the sound pressure in front of the tympanic membrane. This is one reason why there have been few reports on high frequency DPOAE measurements in neonatal rodents, other than that of Mills and Rubel (1996).

ISSN 1499-2027 print/ISSN 1708-8186 online
DOI: 10.1080/14992020902858959

Received:
December 11, 2008
Accepted:
March 1, 2009

Katsuhisa Ikeda
Department of Otorhinolaryngology, Juntendo University School of Medicine, 2-1-1 Hongo, Bunkyo-ku, Tokyo 113-8421, Japan.
E-mail: ike@med.juntendo.ac.jp